Journal of Catalysis **181,** 6–15 (1999)
Article ID jcat.1998.2278, available online at http://www.idealibrary.com on IDEAL®

Carbon Monoxide Oxidation on Copper Oxide Thin Films Supported on Corrugated Cerium Dioxide {111} and {001} Surfaces

Björn Skårman,*[,1] L. Reine Wallenberg,* Per-Olof Larsson,†[,2] Arne Andersson,† Jan-Olov Bovin,* Sissel N. Jacobsen,‡ and Ulf Helmersson‡

*Department of Inorganic Chemistry 2 and †Department of Chemical Engineering II, Lund University, Chemical Center, P.O. Box 124, 221 00 Lund, Sweden; ‡Department of Physics and Measurement Technology, Linköping University, S-581 83 Linköping, Sweden
E-mail: Bjorn.Skarman@oorg2.lth.se

Received April 27, 1998; revised August 10, 1998; accepted September 4, 1998

Thin films of CeO_2 with and without a thin layer of copper oxide were prepared by rf magnetron sputtering on surfaces of α-Al_2O_3 (sapphire) substrates. Careful characterisation of the surfaces was performed down to the atomic level using high-resolution electron microscopy, atomic force microscopy, and X-ray photoelectron spectroscopy. Surprisingly, the as-deposited, corrugated ceria surfaces, nominally (001), consist exclusively of {111}-type lattice planes, but, upon annealing at 800°C, a well-defined portion of (001) surfaces are formed. Oxidation of carbon monoxide to carbon dioxide was studied, having the prepared films in a stirred batch reactor. A batch reactor was chosen so that the conversion over the small sample surface area (ca 10^{-4} m^2) could be monitored as a function of the reaction time. The activity of copper oxide on annealed ceria surfaces is markedly higher than on nonannealed surfaces, indicating a favourable synergetic effect between the ceria (001) surface and the copper oxide phase.

INTRODUCTION

Catalytic activity and selectivity of gas phase reactions on solid surfaces are known to vary substantially with the crystallographic type of surface at which the reaction takes place. This effect is termed structure-sensitivity (1) or catalytic anisotropy (2) and, in principle, it may include synergetic effects created by epitaxial relations between a support and a thin layer of active phase. In the latter case, studies presented in the literature have been focused on the enhancement of the catalytic property caused by the formation of active isolated oxide species or a two-dimensional oxide layer on the support surface. A good example in this regard is the vanadia–titania system for the partial oxidation of hydrocarbons, where various types of dispersed species have been found to be active (3). However, another factor of relevance for the synergy observed in this system, concerns the possibility of having oriented growth of crystalline V_2O_5 atop of anatase (4, 5).

By using structure-directed synthesis, the formation of ideal catalyst surfaces can be approached, where the highly active surfaces are enhanced and the surfaces promoting side-reactions are suppressed. However, a problem with most catalyst supports being used today is that a large specific surface area is desired. As a consequence, the crystallites are very small and irregular, with surfaces that represent a mixture of crystallographic orientations. Using a support with such morphology makes it difficult to single out the support surface that is the most effective for the active phase. In physical vapour deposition (PVD) techniques the possibility exists of manufacturing well-oriented crystal surfaces of oxides, nitrides, and metals with sufficient surface area to produce detectable amounts of product molecules in a catalytic reaction. This is important in particular for oxide catalysts which usually, compared to metal catalysts, have considerably lower turnover frequencies.

Ceria (CeO_2) has attracted attention in catalysis for its properties in automotive exhaust catalysts, where it is added in significant amounts. The role of ceria in this regard concerns its property as a transient oxygen storage medium (6, 7), and the ceria also improves the thermal stability of both the alumina support (8) and the active metals, platinum and rhodium (9). Recently, structure-sensitivity of formic and acetic acid dissociation on ceria (10), as well as CO oxidation on a Rh-CeO_2 combination (11–13) were investigated using oriented thin films, but without atomic scale characterisation by HREM (high-resolution electron microscopy). Moreover, in a comprehensive investigation (14) the Cu-Ce-O system was identified as being one of the most active catalyst systems for the combustion of CO and methane. Only a small amount of copper (2 at%) was needed to obtain a catalyst with high activity. Copper oxide in excess contributed little to the activity and even had a

[1] Corresponding author.
[2] Present address: Perstorp Catalysts, Perstorp AB, S-284 80 Perstorp, Sweden.

0021-9517/99 $30.00

detrimental effect when water vapour was present (15). We therefore considered it worthwhile to investigate a possible catalytic anisotropy and the synergetic effect between the copper oxide phase and the ceria surface.

METHODS

Catalyst Preparation

The CeO_2 thin films were deposited on an *r*-plane(1$\underline{1}$02) sapphire (α-Al_2O_3) substrate in an rf magnetron sputtering system using an off-axis target to substrate configuration. A pressed CeO_2 target (99.9% purity, ∅50 mm) was used for the deposition. Before each deposition, the target was presputtered for 15 min with the substrate shutter closed to achieve stable conditions. The vacuum chamber was pumped by a turbo molecular pump producing a base pressure of 9.3×10^{-5} Pa, which was raised to 14.6 Pa by admitting a mixture of Ar and O_2 at a volume ratio of 3 : 1. The $10 \times 10 \times 0.5$-mm sapphire substrate was mounted on a resistively heated substrate holder using a small amount of silver paste. During the sputtering, the temperature was kept at about 800°C and the rf power on the target was 100 W, operating at 13.56 MHz, yielding a growth rate of about 5.0 nm min^{-1}. After deposition, the films were cooled to room temperature in 50.65 kPa O_2 over the course of 100 min. Films with thickness in the range 140–300 nm were produced and for catalysis experiments a thickness of 300 nm was selected. All samples for the present investigation were grown on sapphire substrates from the same batch and at identical process conditions. Two of the as-deposited samples were further annealed in an $Ar : O_2$ (3 : 1) atmosphere (14.6 Pa) at 800°C for 90 min.

As-deposited, as well as annealed, CeO_2 layers were deposited with copper simultaneously to ensure identical conditions. Thin layers of ∼8 monolayers Cu were grown by rf magnetron sputtering from a disk-shaped ∅50 mm metallic target, also using an off-axis geometry. The Cu films were deposited at room temperature (∼25°C) using an rf power of 20 W in a pure Ar atmosphere, kept at a total pressure of ∼0.7 Pa during the process. The resulting growth rate was measured to approximately 5 nm min^{-1}. The thin layers of metallic Cu are then rapidly oxidised to CuO_x when exposed to air (16).

Reference catalysts were prepared by impregnating polycrystalline TiO_2 (anatase) and CeO_2 supports with an appropriate amount of an aqueous solution of copper nitrate. After the impregnation these catalysts were dried for 16 h at 80°C and finally calcined in air at 500°C for 4 h. The prepared CuO_x/TiO_2 and CuO_x/CeO_2 catalysts with a loading of 12 μmol Cu/m^2 surface area of the support had specific surface areas of 34 $m^2\ g^{-1}$ and 1.5 $m^2\ g^{-1}$, respectively. The catalysts were ground to <150 μm before they were tried for the oxidation of CO.

High Resolution Electron Microscopy (HREM)

To avoid artefacts from conventional mechanical and ion-beam thinning techniques for transmission electron microscope samples, fragments of the copper/ceria oxide films on alumina substrates were prepared by using the small angle cleaving technique (17). The fragments were mounted sideways on a single hole copper grid, such that a profile view of the top surface was enabled. Samples were investigated in a JEM 4000EX high resolution transmission electron microscope (HRTEM). The microscope has a structural resolving power of 0.16 nm at an accelerating voltage of 400 kV and is equipped with an image intensified TV-rate camera and a slow-scan CCD camera for direct digital recording.

X-ray Photoelectron Spectroscopy (XPS)

X-ray photoelectron spectroscopy analyses were performed on a Kratos XSAM 800 spectrometer. The recordings were performed with MgKα radiation (1253.6 eV). The anode was operated at an accelerating voltage of 13 kV and a current of 19 mA. The residual pressure inside the spectrometer was 1.3×10^{-6} Pa, or lower. Charging effects were corrected by adjusting the C 1s peak to a position of 285.0 eV.

Due to photoreduction of dispersed copper oxide in the spectrometer (14, 18) the analysis of each sample was initiated with single scan analysis of the Cu 2p, Ce 3d, C 1s, and O 1s regions, in that order (12.5 min), followed by wide-scan analysis (5 min) between 0–1100 eV binding energy. In both cases the pass energy was 80 eV at high magnification. Finally, multiscan recording was performed of the selected regions with a pass energy of 40 eV at high magnification.

Atomic Force Microscopy (AFM)

Atomic force microscopy measurements were performed at ambient room conditions using a commercial Nanoscope III scanning probe microscope (Digital Instruments). The instrument was operated in tapping mode using silicon cantilevers (Oriel GmbH) oscillating at a resonance frequency between 238–244 kHz. The measurements were carried out on 1×1 μm areas. The mean roughness, R_a, is defined as the mean value of the surface roughness relative to the centre plane. The centre plane is a calculated plane, based upon the surface data, and has equal volume (bounded by the surface) above and below the plane. The peak-to-valley roughness, R_{max}, is defined as the difference between the highest and lowest points, relative to the centre plane within the scanned area. R_a and R_{max} were measured over 1×1 μm scan fields. The surface roughness obtained by AFM is lower than the true value, due to the fact that the diameter of the AFM tip is about 10 nm at its best, and thus, it cannot track the fine details of the surface.

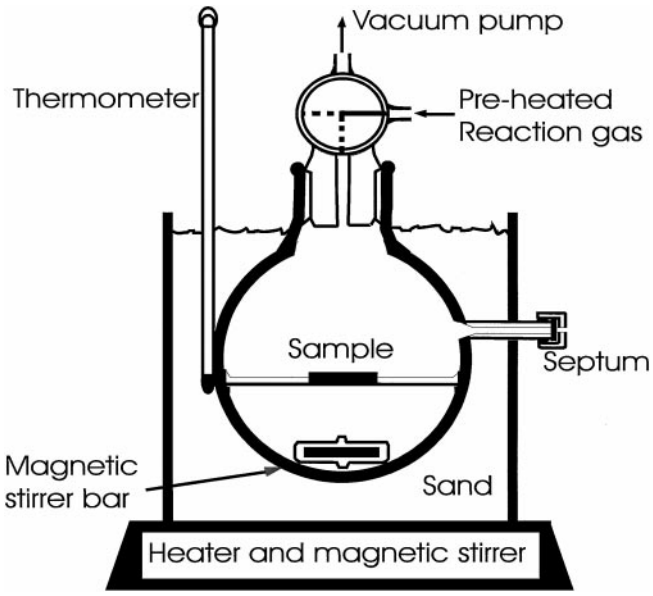

FIG. 1. The catalytic measurements were performed in a stirred glass batch reactor embedded in a heated sand bath. The sample was placed on a glass grid at the centre of the reactor.

Carbon Monoxide Oxidation

The catalytic measurements were performed using a heated batch reactor made of glass and with a total volume of 105.4 ml (Fig. 1). The reactor was embedded in a sand bath on top of a combined heater and magnetic stirrer (Heidolph MR 2002). A glass-embedded magnetic stirrer bar provided the gas convection inside the reactor. The temperature was kept at $270 \pm 2^{\circ}$C, as measured by a thermometer adjacent to the external wall of the reactor. The reaction gas mixture, consisting of 0.991 ± 0.02 vol% CO in synthetic air ($N_2 : O_2$ (4 : 1)), was preheated through a stainless steel coil which was embedded in the sand bath outside the reactor. A three-way valve made it possible to evacuate and fill the reactor repeatedly before the start of each experiment. The partial pressure of CO at the start was approximately 990 Pa at 270°C; i.e., the reactor contained 23 μmol CO, assuming ideal behaviour.

Gas Composition Analysis

A Varian 3400 gas chromatograph (GC) equipped with a flame ionisation detector (FID) was used to analyse the gas composition. The separation of the carbon oxides was accomplished at 65°C using a 2 m $\times$ 1/8 in. stainless steel column filled with Porapak N, 80/100 mesh. A second column, 4 cm $\times$ 1/8 in., was connected in series and was filled with 2% Ni on acid-washed Chromosorb G, 80/100 mesh. This column was kept in a separate oven at 370°C and was used for converting the carbon oxides quantitatively into methane in the presence of hydrogen before the detector (19–21). All gas samples were taken through a septum and were manually injected into the GC. The conversion of carbon monoxide was followed over time and was calculated according to

$$\text{Conversion of CO} = \frac{A_{CO_2}}{(A_{CO} + A_{CO_2})} \times 100\%,$$

where A_{CO} and A_{CO_2} are the integrated peak areas of carbon monoxide and carbon dioxide being detected as methane, respectively.

RESULTS

High Resolution Electron Microscopy

The high resolution electron micrographs show the nominal {001} oriented, as-deposited ceria film to be strongly corrugated over the whole surface, see Fig. 2. Two types

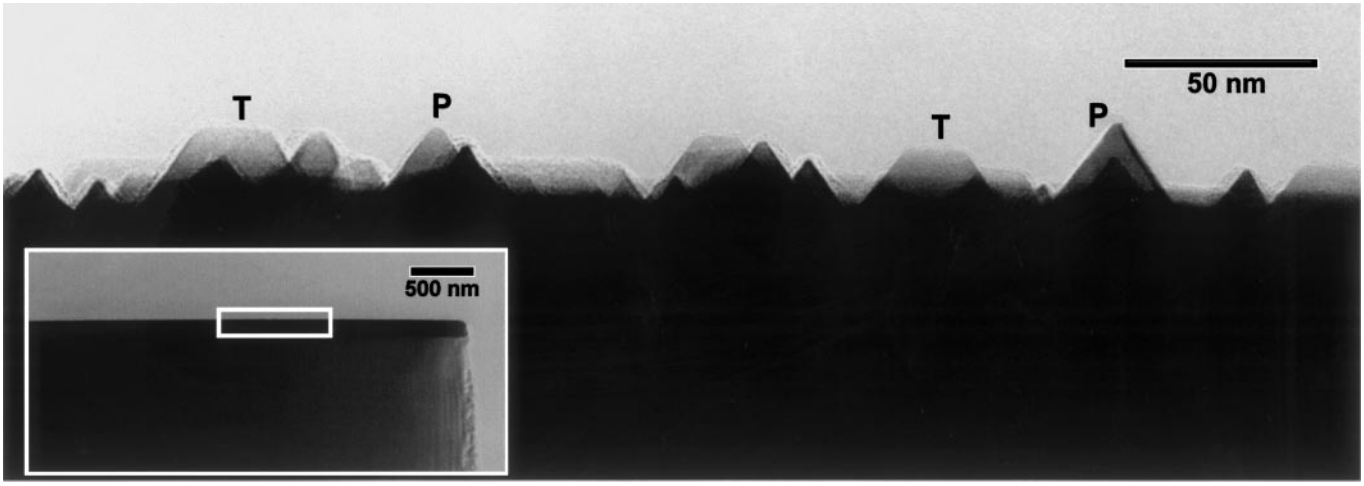

FIG. 2. Profile view of as-deposited ceria showing pointed (P) and trapezoidal (T) surface features. The inset, at lower magnification, shows the cleaved crossection of the ceria film, with a thickness of 140 nm, grown on sapphire.

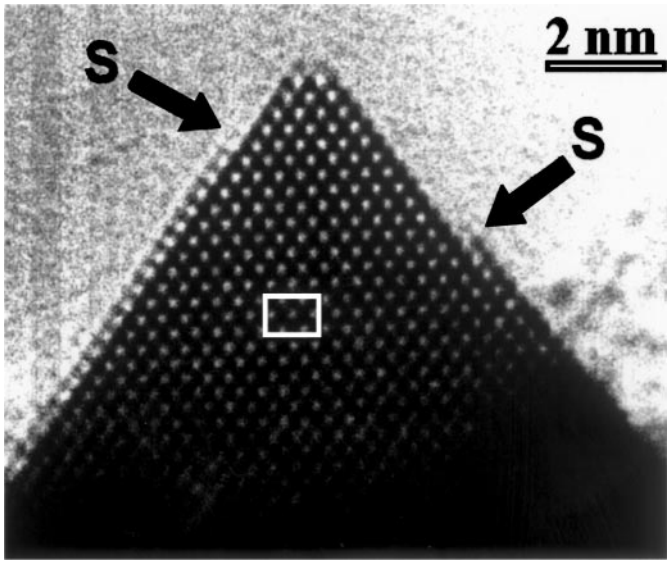

FIG. 3. As-deposited ceria viewed along the [110] of the cubic lattice. Dark spots correspond to heavy cerium ion positions, which form a face-centred cubic unit cell in the fluorite structure type (inset). The slopes of the pointed peak expose {111}-type lattice planes, where occasionally incomplete surface layers show up as surface steps (S).

of features can be seen protruding from the surface: trapezoidal (T) or "hut shaped" crystallites, and sharply pointed (P) crystallites. Typical examples of these are indicated in the figure. The inset shows the whole thickness of the ceria film (140 nm) on top of the α-Al_2O_3 substrate. In the thin part of the wedge-shaped sample, the ceria film appears as a darker slab, due to the higher scattering power for electrons, compared to α-Al_2O_3. At insufficient magnification and resolution, both the ceria interface towards the substrate and the microscope vacuum appear smooth, but only the ceria/alumina interface is atomically flat. Enlargement of the boxed area in the inset shows the real surface structure to be corrugated with an amplitude of approximately 10% of the average film thickness.

The trapezoidal and pointed peaks are only sharply visible simultaneously when viewing exactly along the [$\underline{1}$10] direction of the cubic ceria lattice, or in a direction perpendicular to that in the surface plane. Figure 3 shows a HREM image of a pointed peak viewed in this direction. The dark spots correspond to the heavy cerium ion positions, which form a face-centred cubic lattice in the fluorite structure type. The much lighter oxygen ions, which form a simple cubic lattice, give little contribution to the scattering. The pointed peaks are extremely sharp, with an edge "bluntness" usually between $\frac{1}{2}$–2 unit cells (2–5 cerium atoms). The slopes of the peak are formed by {111}-type lattice planes, which correspond to close-packed planes in the cation lattice. In general, the surfaces are atomically flat, but occasional incomplete surface layers show up as surface steps, $\frac{1}{3}$ of a unit cell in height (marked S in Fig. 3).

After annealing at 800°C, all sharply pointed peaks have disappeared, and only trapezoidal surface features remain, as shown in Fig. 4. The termination at the top surface is clearly more abrupt than for the trapezoidal features found before annealing. A levelling effect on the surface is obvious from the images, which can also be disclosed as a slight decrease in the average corrugation amplitude measured from overview images. The HREM images provide strong evidence that the two surface features (T and P in Fig. 2) are merely two different views of morphologically very

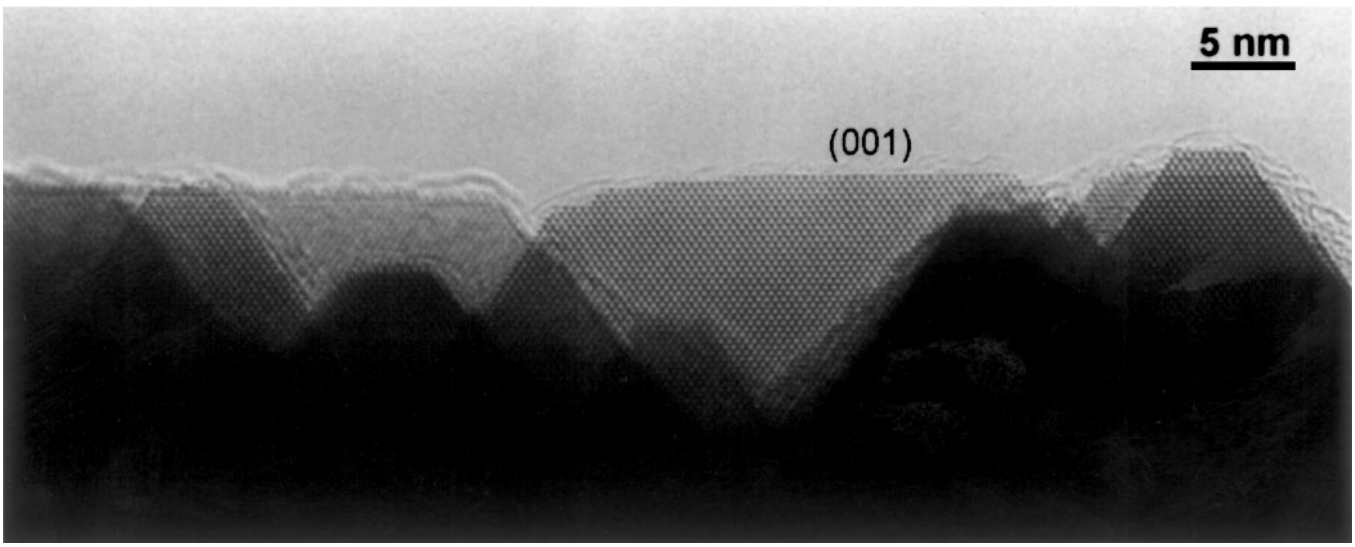

FIG. 4. HREM profile view of an annealed ceria film. All sharply pointed peaks have disappeared by truncation. The termination at the top surface is clearly more abrupt than for the trapezoidal features before annealing, indicating the (001)-type lattice planes at the top surface. Note that the {111}-type slopes are still dominating the total surface area.

similar objects. Three-dimensional model construction reveals the unexpected fact that the exposed as-deposited surface, which nominally is a {001} type surface, actually consists entirely of {111} type facets. It is equally clear that the annealing procedure produces a fraction of (001) surfaces, which are parallel to the substrate/CeO_2 interface by truncation of the ridges. Further evidence of the exact shape derived from tilt experiments and detailed discussions on factors governing the as-deposited and annealed shapes are given elsewhere (22).

Figures 5a and 5b show the as-deposited ceria and annealed ceria surfaces, respectively, after approximately eight monolayers of copper deposition. An amorphous overlayer of about 2-nm thickness is present in both cases. A few crystalline particles could be found, as shown in Fig. 5b, but not frequently enough to account for all deposited copper and without any obvious epitaxial relationship to the ceria support.

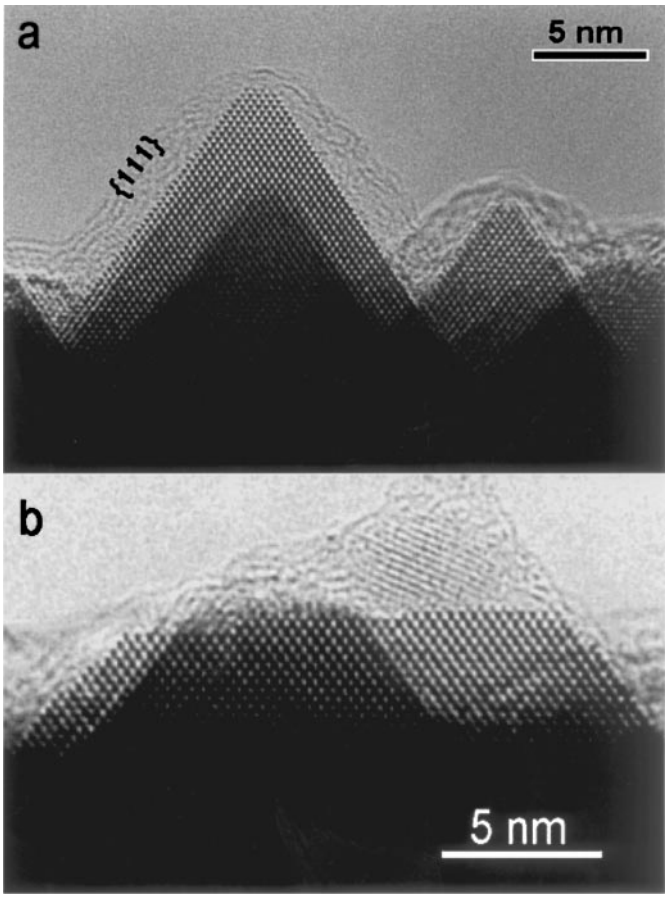

FIG. 5. Ceria surfaces after approximately eight monolayers of copper deposition. An amorphous overlayer of about 2-nm thickness is present in both cases: (a) as-deposited ceria surface, with predominantly {111} facets; (b) annealed ceria film with a crystalline particle. Possible phases of the particle might be Cu_2O, Cu_4O_3, or CuO.

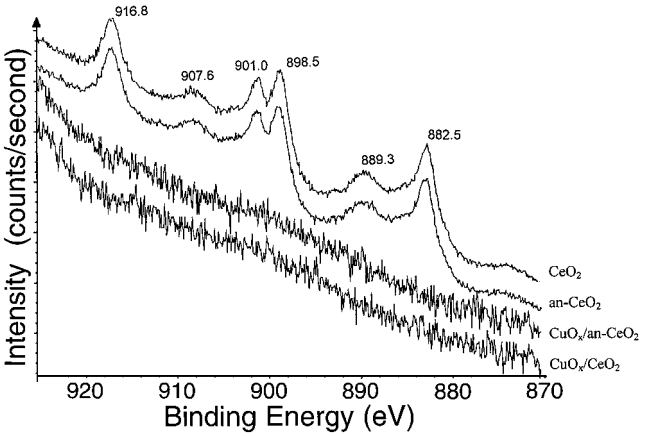

FIG. 6. XPS spectra of the Ce 3d region for the as-deposited and annealed CeO_2 samples with and without a CuO_x layer. (The spectrum intensity for the pure ceria samples has been multiplied with a factor 0.17). Multiscan analysis with a pass energy of 40 eV at high magnification.

X-ray Photoelectron Spectroscopy (XPS)

Wide scan analysis between 0 and 1100 eV binding energy for the as-deposited and annealed ceria samples showed the presence of Ce, O, and C. For the copper deposited samples wide scan analysis showed the presence of Cu, O, and C. No other elements were detected.

Figure 6 shows the Ce 3d region for the four samples. The as-deposited and annealed ceria samples show the typical CeO_2 spectra with peak maxima at 882.5, 889.3, 898.5, 901.0, 907.6, and 916.8 eV. These values are in good agreement with the values obtained by Jin *et al.* (23) after oxidation treatment. The outlines of the CeO_2 spectra in the Ce 3d region and the positions of the peaks are also in good agreement with the results obtained by several other authors (24–28). The peaks at 882.5, 889.3, and 898.5 eV have been attributed to Ce $3d_{5/2}$ states and the peaks at 901.0, 907.6, and 916.8 eV to Ce $3d_{3/2}$ states (23, 25). Upon reduction the peaks at 889.3 and 907.6 eV decreased in intensity and two new peaks appeared at 885.9 and 904.4 eV, corresponding to Ce $3d_{5/2}$ and Ce $3d_{3/2}$ states, respectively, increasing in intensity with increased degree of reduction (23). It is also reported (24, 26) that, in combination with the growth of these peaks, the relative area of the peak around 916.8 eV decreased with increased reduction. Consequently, the absence of any peaks around 885.9 and 904.4 eV and the pronounced peak at 916.8 eV indicate the presence of stoichiometric CeO_2 in both the as-deposited and annealed samples. Figure 6 also shows that for the copper-deposited thin films there is no cerium signal present, which indicates complete coverage of the ceria surface with CuO_x.

Figure 7 shows the Cu 2p region (single scan) for the two copper-deposited ceria samples. The peak corresponding to Cu $2p_{3/2}$ is positioned at 934.7 eV and the existence of Cu

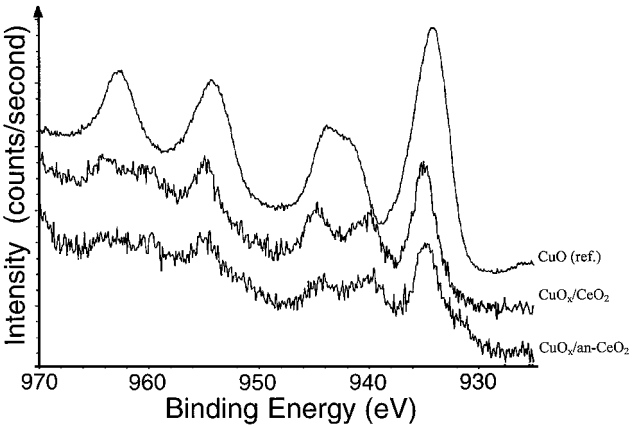

FIG. 7. XPS spectra of the Cu 2p region for the as-deposited and the annealed CeO_2 samples with a CuO_x layer. Single scan analysis with pass energy of 80 eV at high magnification. The spectrum of pure CuO is shown as a reference and the intensity has been multiplied with a factor 0.25.

$2p_{3/2}$ and Cu $2p_{1/2}$ shake-up satellites indicate the presence of Cu^{2+}. However, increased analysis time reduced the intensity of the shake-up satellites due to photoreduction in the spectrometer (14, 18, 29).

Atomic Force Microscopy (AFM)

A set of typical AFM images of a 1-μm^2 area of four studied catalytic surfaces, viewed from above in the [00$\underline{1}$] direction of the cubic ceria lattice, is shown in Figs. 8a–d. The images illustrate the submicron surface roughness and reveal details of the surface morphology, i.e. crystallite size and shape.

Figure 8a shows the as-deposited ceria thin film with crystallite ridges in the [110] and [$\underline{1}$10] directions of the cubic fluorite cell, i.e. two perpendicular directions. This implies that only the {111} type surface is exposed, when taking into consideration observations from the HRTEM investigation (Fig. 3). After annealing at 800°C for 1.5 h (Fig. 8b) the film was still composed of individual, perpendicular crystallites, which essentially show the same apparent sharpness due to tip imaging. However, the film shows a reduction in surface roughness, as indicated by a less distinct appearance in the AFM images. As confirmed by the HRTEM results (Fig. 4) this decrease of roughness originates from the truncation of the sharp facets into {001} surfaces, giving a mixture of {111} and {001} facets (22, 30).

The R_a and R_{max} values for the four samples are presented in Table 1. The as-prepared ceria film has a distinctively higher R_a-value (3.9 nm) than the annealed ceria film (3.0 nm), which further supports the gradual truncation of sharp ridges into smooth {001}-planes. Figure 8c reveals the morphology of an identical surface to the one in Fig. 8a, but with approximately eight monolayers of postdeposited copper on top. The copper oxide layer gives rise to a smoother surface ($R_a = 3.3$ nm), comparable to the roughness of the annealed surfaces, but with features with an apparent size of 10–15 nm dispersed on the ridge walls. (Particles <10 nm will be imaged as the tip curvature). For the annealed surface, the deposited copper layer does not result in a significantly smoother morphology (Fig. 8d). The surface reveals, however, similar nanosized features as the copper-deposited nonannealed ceria sample (Fig. 8c).

Locally, a higher degree of parallel ordering of the ridges is obvious, which is possibly due to parallel steps on the starting α-Al_2O_3 substrate surface. AFM images did not show any significant changes in the surface morphology after performing catalytic reactions at 270°C for several hours.

Carbon Monoxide Oxidation

In order to ensure reliable and reproducible results for the thin film samples, the sealed glass batch-reactor was first tested with only a substrate sample at 270°C, i.e., a blank experiment. This exhibited a slow oxidation of carbon monoxide with a conversion of $3.0 \pm 0.6\%$ per hour, corresponding to 0.23 ± 0.04 μmol CO m^{-2} s^{-1}, which contributes insignificantly to the total catalytic activity. Figure 9 shows the conversion curves for the substrate and the different CeO_2 thin films.

At the starting point of the catalytic experiments the reactor contains approximately 23 μmol CO in synthetic air. The thin films without copper oxide have an activity comparable to blank experiments. The as-deposited thin film with copper oxide, which expose mainly the CeO_2(111) surface, has a maximum activity of 1.5 μmol CO m^{-2} s^{-1}, which is slightly higher than that of the films without copper. For the annealed sample, exposing a portion of the CeO_2(001) surface, a marked increase in activity is observed when copper oxide is present on top of the ceria surface. This sample converts 94% of the carbon monoxide to carbon dioxide in the reactor within 100 min, corresponding to an average conversion rate of 38 μmol CO m^{-2} s^{-1}. For the first 10 min, the conversion rate is about 90 μmol CO m^{-2} s^{-1}. Considering that only ~1/5 of the height of the sharp crystallite ridges are truncated by annealing, i.e. the (001) portion constitutes approximately 15% of the total surface area, the conversion using a purely (001) support surface would be even higher. For comparison, the specific activities of the various catalysts are presented in Table 2.

TABLE 1

Surface Roughness of the Thin Film CeO_2, with and without a Layer of Copper Oxide

	As-deposited ceria	Annealed ceria	As-deposited ceria with CuO_x	Annealed ceria with CuO_x
R_a [nm]	3.5-4.3	2.7-3.3	3.1-3.5	2.8-3.6
R_{max} [nm]	40 ± 4	28 ± 1	34 ± 3	28 ± 3

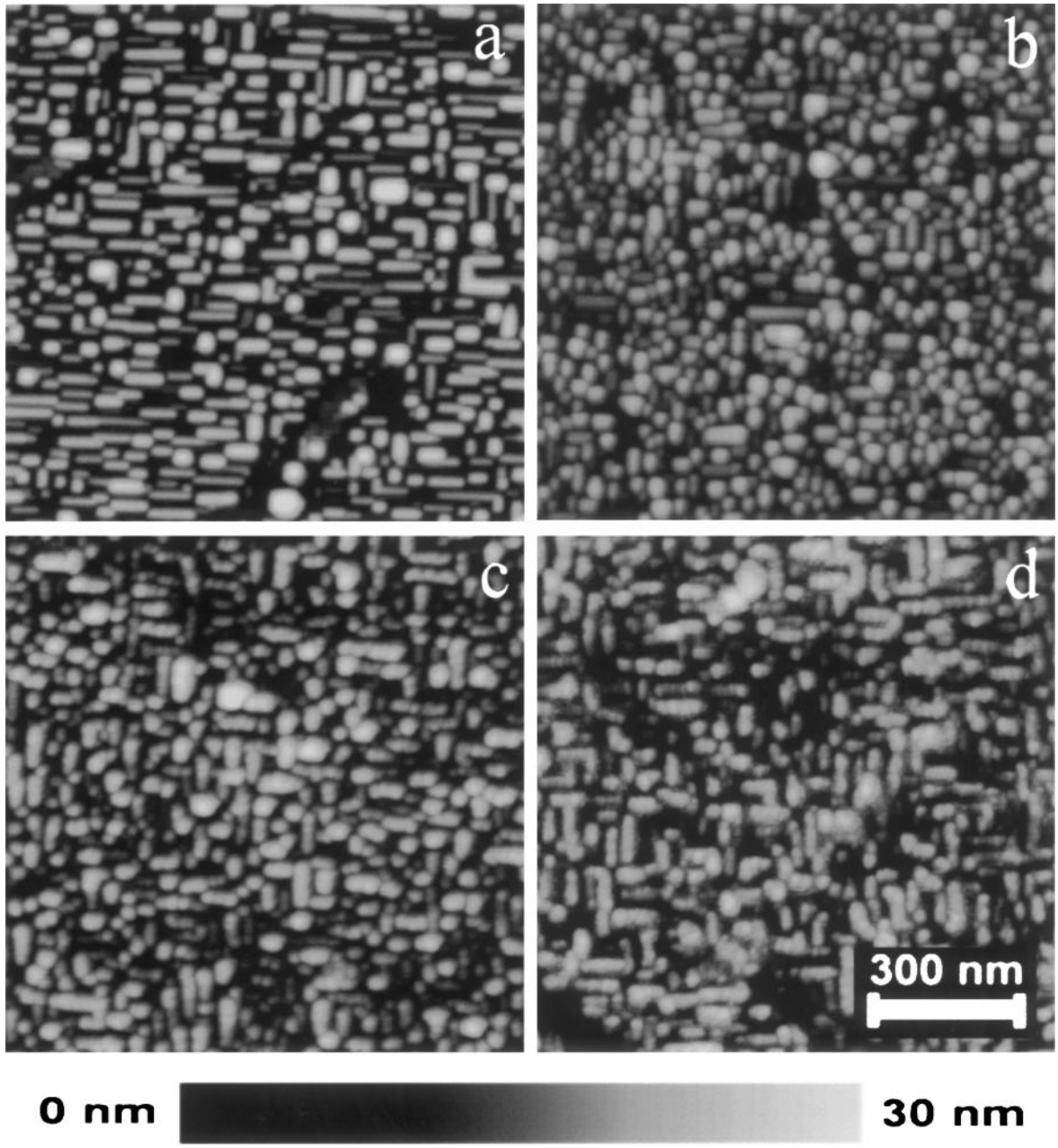

FIG. 8. AFM images of CeO_2 thin films (~300 nm thickness) grown on sapphire. A height scale is shown below the images: (a) as-deposited; (b) annealed in O_2 at 800°C for 90 min; (c) is identical to (a) but with approximately eight monolayers of CuO_x on top; (d) is identical to (b), but with approximately eight monolayers of CuO_x on top.

The activities of the thin film catalysts were compared with those of two samples with monolayer loading of CuO_x on polycrystalline TiO_2 and CeO_2, respectively. The maximum conversion rates for CuO_x/TiO_2 and CuO_x/CeO_2 were determined to be 0.23 ± 0.02 and 0.53 ± 0.02 μmol CO m^{-2} s^{-1}, respectively. Thus, the rate over copper oxide on the annealed ceria surface is almost 170 times higher than for the copper oxide on the polycrystalline support. The difference is partly due to the internal mass transfer limitations that exist using polycrystalline material.

DISCUSSION

Using single crystal surfaces or oriented thin films to study catalytic reactions on specific surfaces is a very promising approach. However, the treatment procedure of the surfaces before use in catalysis and characterisation methods must be taken into special consideration. For CeO_2{111} oriented films (10, 11), the natural tendency to form these surfaces makes simple polishing and annealing procedures sufficient to produce uniform surfaces. For

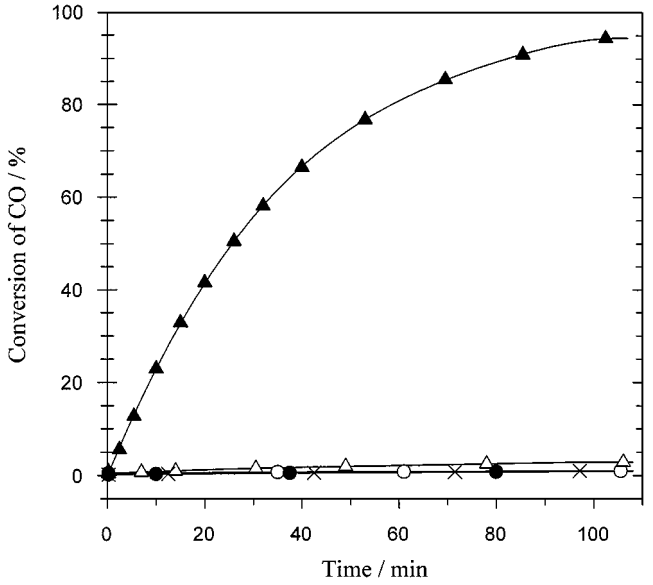

FIG. 9. The conversion of carbon monoxide (0.991% CO in synthetic air) to carbon dioxide at 270°C over four different CeO_2 thin film samples: (—×—) pure sapphire substrate; (—○—) as-deposited CeO_2/substrate; (—●—) annealed CeO_2/substrate; (—△—) as-deposited CeO_2/substrate with copper oxide; and (—▲—) annealed CeO_2/substrate with copper oxide.

sputtered CeO_2\{001\} oriented films, we have confirmed here that the type of exposed surface is highly dependent on details of the annealing procedure. Suitable characterisation methods should be used, since many otherwise very informative methods, e.g. LEEDS, have proven difficult to use on these types of samples due to charging (11). It has been observed (10) that high-resolution electron energy loss spectra (HREELS) are very difficult to obtain from \{001\} oriented films, compared to polished (111)-oriented surfaces. This may be explained by the unexpected topology that we have observed. Combinations of several methods may be necessary to better interpret the results from individual methods. Most characterisation methods need conditions that are far from actual working conditions for the catalyst, and possible effects of surface structures, oxidation states, and vacancy formation should be kept in mind.

TABLE 2

Specific Activities for CO Oxidation over the Various Thin Films and Bulk Catalysts

	Initial rate [μmol m^{-2} s^{-1}]
Sapphire substrate (blank)	0.23
As-deposited ceria	0.2
Annealed ceria	0.2
As-deposited ceria with CuO_x	1.5
Annealed ceria with CuO_x	90
Polycrystalline CuO_x/CeO_2	0.53[a]
Polycrystalline CuO_x/TiO_2	0.23[a]

[a] The examined surface area of the polycrystalline material is approximately 400 times higher than the area of the thin film samples.

By combining the results from HREM and AFM we have obtained a detailed description of the 3D morphology and crystallography of the CuO_x/ceria surface of the film, which in turn can be correlated to the conversion activity for carbon monoxide. Figure 10 shows a schematic drawing of the crystal structure of CeO_2, both before and after annealing, with the direction of the lattice and limiting faces drawn according to the observed topography. Due to the convolution of the comparatively blunt scanning probe (tip radius >10 nm) of the AFM with the surface, the true sharpness of the ridges cannot be conveyed with this method. However, this is clearly established by the HREM images. AFM, on the other hand, proves that the surface structures used for catalysis are uniform over the whole surface and, thus, can be treated with statistical confidence.

After annealing, the sharp ridge edges have disappeared, and detailed analyses of HREM images and tilting to other zone axes (22, 31) prove the controlled formation of (001)

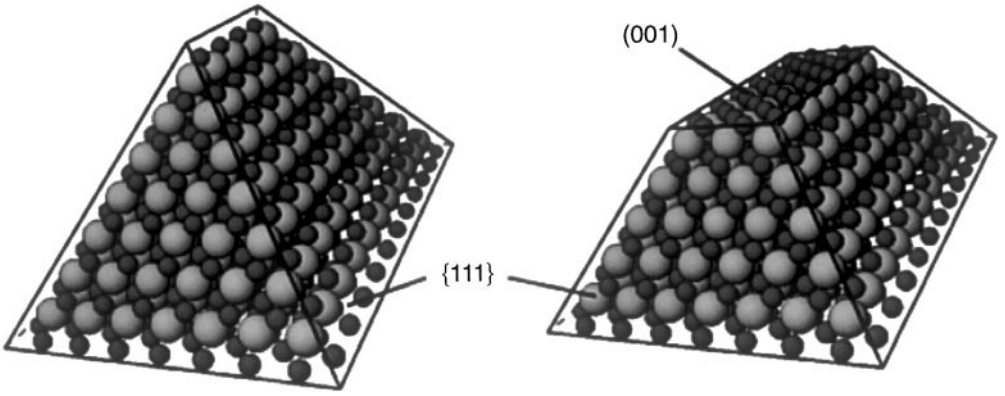

FIG. 10. The fluorite structure of CeO_2 according to the observed topography of the thin film. Large spheres are cerium and small, dark spheres are oxygen. Only \{111\} type surfaces are exposed on the as-deposited CeO_2 (left). After annealing the \{111\} surfaces are still dominating, but a clear truncation by \{001\} facets is present (right). The long axes of the ridges are always parallel to [110] or [$\bar{1}$10] directions.

surfaces by truncation. This is further reflected in the decreased mean surface roughness and maximum corrugation amplitude from AFM, performed over larger areas (Table 1).

In Fig. 10, the surfaces are depicted as being terminated by oxygen. This seems plausible, since the ceria surfaces are exposed to air prior to catalysis. In addition, the XPS spectrum in Fig. 6 shows a clear signature of Ce^{4+}. During catalysis, however, the situation may change in a thin surface region, where a dynamic exchange of oxygen between the gas phase, the copper oxide phase, and the ceria lattice is expected to occur, leaving cerium locally and temporarily in a +3 state. A theoretical calculation (33) indicates that less energy is required to form such anion vacancies on (001) than on (111).

The amorphous overlayer, visible in HREM images (Fig. 5) and indicated in AFM images of surfaces after Cu-deposition (Figs. 8c, d), is not unequivocally determined. This could be either amorphous CuO_x, or simply adsorbed amorphous carbon. Amorphous carbon and other debris accumulate on the surfaces with time as the samples are exposed to air. To remove loosely adsorbed species, the samples were left in the microscope vacuum ($\sim 10^{-5}$ Pa) for several hours before viewing, but a significantly thicker remaining amorphous overlayer could be observed in cases where Cu was present. XPS, performed under UHV conditions, shows that there is a clear Cu 2p signal but no Ce 3d signal (Figs. 6 and 7), indicating that the surface is completely covered with a copper-containing phase. On the other hand, there is also a higher (approx. 50 at%) carbon C 1s signal after deposition of copper. The few CuO_x crystalline particles found on the surface (Fig. 5b) cannot account for the total amount of copper deposited. The lattice spacing of the particle in Fig. 5b was determined to be 2.4 ± 0.1 Å, using the known spacing and orientation of the support. Complete reduction to metallic copper can be excluded ($d_{111}(Cu) = 2.09$ Å), even when considering reports of an expansion of the lattice in small particles ($d_{111}(Cu) \approx 2.12$ Å) (16). The spacing is, however, compatible with spacings in copper oxides, e.g. $d_{111}(Cu_2O) = 2.46$ Å and $d_{111}(CuO) = 2.32$ Å (34), but the limited particle size prevents an accuracy sufficient to exclude any of the two most common forms of copper oxide. XPS Cu 2p spectra have a signature revealing that copper is present in the +2 state (Fig. 7). This leads to the conclusion that copper is predominately present as part of the amorphous layer, which may crystallise epitaxially on the ceria surface during the catalysis experiments. It is likely that partial changes in the oxidation state and surface structure are introduced before stable working conditions for the catalytic reaction are reached. Judging from our previous experience of surface phases in the VO_x/TiO_2 system (35), such changes are very difficult to prove unambiguously by examining the catalyst after use. The problem in this regard concerns the known fact that reduction of supported copper oxide is facile under vacuum (18) and, therefore, it can be reduced in the electron microscope. Moreover, during use in the CO oxidation, carbon can accumulate on the surface, which will complicate the interpretation of electron micrographs of the surface. It would, thus, be preferable to perform *in-situ* characterisation during catalysis. This is a task, which we will pursue for future investigations. However, we would like to present a hypothesis here which is worth considering as an explanation for the improved activity and the synergetic effect that is induced by the ceria.

When trying to understand and interpret the measured catalytic data, two central questions evolve:

i. What causes the synergetic effect that has been observed between ceria and the copper containing phase (14, 15)?

ii. Why is copper oxide more active on $CeO_2(001)$ than on $CeO_2(111)$?

When addressing the first question, we can imagine an epitaxial copper oxide phase on top of the fluorite type CeO_2. Starting with fcc copper metal, the oxidation process can be structurally derived simply by successive insertion of oxygen into empty tetrahedral sites. This will take us through the three copper oxide forms: cuprite (Cu_2O, cubic) (34, 36); paramelaconite (Cu_4O_3, tetragonal, mixed valence) (37); and tenorite (CuO, monoclinic) (34, 38). An epitaxial relationship is not obvious, due to the difference in unit cell description. However, since the cation lattice is essentially maintained, we can recalculate and compare appropriate cation lattice dimensions. We find a tensile strain imposed on the copper oxides by the ceria support, which diminishes from 27% lattice misfit for cuprite to around 8% as more oxygen atoms are inserted into the cell going to tenorite. Misfit strain of this magnitude can only be maintained for a few monolayers, e.g. the approximately eight monolayers of copper used in the catalysts examined here, before dislocations or other disruptions of the structure occur spontaneously. The end point member of the oxides, tenorite, where all Cu is in the +2 state, imposes a strong monoclinic distortion of the unit cell, which makes it unlikely that the epitaxial relationship can be maintained, and it will break loose from the support. This is supported by the finding (14), that bulk ceria/Cu catalysts with a copper content exceeding 8% produce X-ray diffraction lines of tenorite, but give no improvement in catalytic behaviour.

Addressing the second question, we suggest that the drastically improved activity of copper oxide on $CeO_2(001)$ surfaces is due to the greater ability of this ceria surface, compared to $CeO_2(111)$, to assist the copper oxide in changing valence and supplying oxygen. Having copper partly in the +1 state has previously been reported to be essential for the catalytic activity (14, 15, 39). It is likely that a rapid change

in valence state between +1 and +2, while maintaining the basic lattice, is a crucial part of the reaction mechanism. It may be worth noting that the paramelaconite structure (37) has alternating rows of Cu^{+1} and Cu^{+2} with a 90° twist between the layers, and that cuprite is an *n*-type semiconductor with high lattice charge mobility.

Another structural aspect of importance to the system is the possibility of partially reducing the ceria support, through donation of mobile oxygen to the copper oxide, without inflicting large structural changes or phase transitions of the fluorite structure. Previously, stable Ce_2O_3 with a hexagonal structure has been identified, but it is well known that Ce^{4+} in the fluorite lattice can be successively replaced by several rare earth metals over the whole composition range, leading to the cubic C-type sesquioxide structure (bixbyite), which is only a slight perturbation of the fluorite structure (40, 41). However, there is no reason why this cannot be achieved by partly reducing Ce^{4+} to Ce^{3+}, giving a C-type structure directly. There have been some indications of an existing surface phase with this structure (39).

CONCLUSION

Through combining several characterisation techniques like HREM, AFM, and XPS, we have confirmed down to atomic resolution that the topology of (001)-oriented CeO_2 thin films, produced by rf-magnetron sputtering have only \{111\} surfaces exposed, but that (001) surfaces can be introduced through annealing. Sputter deposition of the nominal eight monolayers of metallic copper is sufficient to reach complete surface coverage.

In relation to the previously reported synergy between copper oxide and CeO_2 for CO oxidation (14, 15), we have shown for the first time that copper oxide is considerably more active on CeO_2(001) than on CeO_2(111).

REFERENCES

1. Boudart, M., *in* "Advances in Catalysis" (D. D. Eley, H. Pines, and P. B. Weisz, Eds.), Vol. 20, p. 153. Academic Press, New York, 1969.
2. Ziólkowski, J., *J. Catal.* **80**, 263 (1983).
3. Sanati, M., and Andersson, A., *J. Mol. Catal.* **59**, 133 (1990).
4. Véjux, A., and Courtine, P., *J. Solid State Chem.* **23**, 93 (1978).
5. Kang, Z. C., and Bao, Q. X., *Appl. Catal.* **26**, 251 (1986).
6. Yao, H. C., and Yao, Y. F., *J. Catal.* **86**, 254 (1984).
7. Logan, A. D., and Shelef, M., *J. Mater. Res.* **9**, 468 (1994).
8. Harrison, B., Diwell, A. F., and Hallett, C., *Platinum Met. Rev.* **32**, 73 (1988).
9. Summers, J. C., and Ausen, S. A., *J. Catal.* **58**, 131 (1979).
10. Stubenrauch, J., Brosha, E., and Vohs, J. M., *Catal. Today* **28**, 431 (1996).
11. Stubenrauch, J., and Vohs, J. M., *J. Catal.* **159**, 50 (1996).
12. Putna, E. S., Vohs, J. M., and Gorte, R. J., *J. Phys. Chem.* **100**, 17862 (1996).
13. Stubenrauch, J., and Vohs, J. M., *Catal. Lett.* **47**, 21 (1997).
14. Liu, W., and Flytzani-Stephanopoulos, M., *J. Catal.* **153**, 304 (1995) (Part I, II).
15. Liu, W., and Flytzani-Stephanopoulos, M., *Chem. Eng.* **64**, 283 (1996).
16. Urban, J., Sack-Kongehl, H., and Weiss, K., *Z. Phys. D* **36**, 73 (1996).
17. McCaffrey, J. P., *Microsc. Res. Techn.* **24**, 180 (1993).
18. Larsson, P.-O., Andersson, A., Wallenberg, L. R., and Svensson, B., *J. Catal.* **163**, 279 (1996).
19. Williams, F. W., Woods, F. J., and Umstead, M. E., *J. Chromatog. Sci.* **10**, 570 (1972).
20. Andersson, A., and Hansen, S., *J. Catal.* **114**, 332 (1988).
21. Bunluesin, T., Cordatos, H., and Gorte, R. J., *J. Catal.* **157**, 222 (1995).
22. Jacobsen, S. N., Helmersson, U., Wallenberg, L. R., Erlandsson, R., and Skårman, B., *Surf. Sci.* (1998), in press.
23. Jin, T., Zhou, Y., Mains, G. J., and White, J. M., *J. Phys. Chem.* **91**, 5931 (1987).
24. Wrobel, G., Lamonier, C., Bennani, A., D'Huysser, A., and Aboukaïs, A., *J. Chem. Soc. Faraday Trans.* **92**, 2001 (1996).
25. Laachir, A., Perrichon, V., Badri, A., Lamotte, J., Catherine, E., Lavalley, J., El Fallah, J., Hilaire, L., Le Normand, F., Quéméré, E., Savion, G., and Touret, O., *J. Chem. Soc., Faraday Trans.* **87**, 1601 (1991).
26. Graham, G. W., Schmitz, P. J., Usmen, R. K., and McCabe, R. W., *Catal. Lett.* **17**, 175 (1993).
27. Belton, D. N., and Schmieg, S. J., *J. Vac. Sci. Technol. A* **11**(4), 2330 (1993).
28. Guo, S., Arwin, A., Jacobsen, S. N., Järrendahl, K., and Helmersson, U., *J. Appl. Phys.* **77**, 5369 (1995).
29. Frost, D. C., Ishitani, A., and McDowell, C. A., *Mol. Phys.* **24**, 861 (1972).
30. Guo, S., Jacobsen, S. N., Helmersson, U., Järrendahl, K., Madsen, L. D., Tengvall, P., and Arwin, H., *Mat. Res. Soc. Symp. Proc.* **355**, 209 (1995).
31. Wallenberg, L. R., Jacobsen, S. N., Erlandsson, R., Helmersson, U., Bovin, J.-O., and Andersson, A., *in Proc. European Congr. on Microscopy, Dublin, Ireland, 1996.*
32. Creaser, D. A., Harrison, P. G., Morris, M. A., and Wolfindale, B. A., *Catal. Lett.* **23**, 13 (1994).
33. Conesa, J. C., *Surf. Sci.* **339**, 337 (1995).
34. Long, N. J., and Petford-Long, A. K., *Ultramicrosc.* **20**, 151 (1986).
35. Sanati, M., Wallenberg, L. R., Andersson, A., Jansen, S., and Tu, Y., *J. Catal.* **132**, 128 (1991).
36. Neuburger, M. C., *Z. Krist.* **31**, 169 (1931).
37. O'Keeffe, M., and Bovin, J. O., *Am. Mineral.* **63**, 180 (1978).
38. Yang, J. C., Yeadon, M., Olynick, D., and Gibson, J. M., *Microsc. Microanal.* **3**, 121 (1997).
39. Ying, J. Y., and Tschöpe, A., *Chem. Eng. J.* **64**, 225 (1996).
40. Wallenberg, R., Withers, R. L., Bevan, D. J. M., Thompson, J. G., and Hyde, B. G., *J. Less Com. Met.* **156**, 1 (1989).
41. Withers, R. L., Thompson, J. G., Gabbitas, N., Wallenberg, L. R., and Welberry, T. R., *J. Solid State Chem.* **120**, 290 (1995).